Biomaterials Science

ROYAL SOCIETY OF CHEMISTRY

PAPER

View Article Online
View Journal | View Issue



Cite this: *Biomater. Sci.*, 2023, **11**, 6834



# ICAM-1-decorated extracellular vesicles loaded with miR-146a and *Glut1* drive immunomodulation and hinder tumor progression in a murine model of breast cancer†

Silvia Duarte-Sanmiguel,[a] Ana I. Salazar-Puerta,[a,b] Ana Panic,[a] Daniel Dodd,[a,c] Carlie Francis,[a] Diego Alzate-Correa,[a,b] Lilibeth Ortega-Pineda,[a] Luke Lemmerman,[a] Maria A. Rincon-Benavides,[a,b,d] Kavya Dathathreya,[a] William Lawrence,[a,c] Neil Ott,[a] Jingjing Zhang,[e] Binbin Deng,[f] Shipeng Wang,[a] Sandra P. Santander,[g] David W. McComb,[f,h] Eduardo Reategui,[e] Andre F. Palmer,[e] William E. Carson,[i] Natalia Higuita-Castro*[a,b,d,i,j,k] and Daniel Gallego-Perez*[a,b,d,i,j]

Tumor-associated immune cells play a crucial role in cancer progression. Myeloid-derived suppressor cells (MDSCs), for example, are immature innate immune cells that infiltrate the tumor to exert immunosuppressive activity and protect cancer cells from the host's immune system and/or cancer-specific immunotherapies. While tumor-associated immune cells have emerged as a promising therapeutic target, efforts to counter immunosuppression within the tumor niche have been hampered by the lack of approaches that selectively target the immune cell compartment of the tumor, to effectively eliminate "tumor-protecting" immune cells and/or drive an "anti-tumor" phenotype. Here we report on a novel nanotechnology-based approach to target tumor-associated immune cells and promote "anti-tumor" responses in a murine model of breast cancer. Engineered extracellular vesicles (EVs) decorated with ICAM-1 ligands and loaded with miR-146a and *Glut1*, were biosynthesized (*in vitro* or *in vivo*) and administered to tumor-bearing mice once a week for up to 5 weeks. The impact of this treatment modality on the immune cell compartment and tumor progression was evaluated *via* RT-qPCR, flow cytometry, and histology. Our results indicate that weekly administration of the engineered EVs (*i.e.*, ICAM-1-decorated and loaded with miR-146a and *Glut1*) hampered tumor progression compared to ICAM-1-decorated EVs with no cargo. Flow cytometry analyses of the tumors indicated a shift in the phenotype of the immune cell population toward a more pro-inflammatory state, which appeared to have facilitated the infiltration of tumor-targeting T cells, and was associated with a reduction in tumor size and decreased metastatic burden. Altogether, our results indicate that ICAM-1-decorated EVs could be a powerful platform nanotechnology for the deployment of immune cell-targeting therapies to solid tumors.

Received 6th April 2023,
Accepted 13th August 2023

DOI: 10.1039/d3bm00573a

rsc.li/biomaterials-science

## Introduction

Tumor-associated immune cells play a crucial role in modulating cancer progression.[1,2] Cancer immunosuppression consists of a reduction in the function of the immune system against tumors.[3] This immune modulation is driven, in part, by a group of immature and mature myeloid cells that reside in the tumor microenvironment, including myeloid-derived

[a]*The Ohio State University, Department of Biomedical Engineering, Columbus, OH 43210, USA. E-mail: gallegoperez.1@osu.edu, higuitacastro.1@osu.edu*
[b]*The Ohio State University, Gene Therapy Institute, Columbus, OH 43210, USA*
[c]*The Ohio State University, Biomedical Sciences Graduate Program, Columbus, OH 43210, USA*
[d]*The Ohio State University, Biophysics Program, Columbus, OH 43210, USA*
[e]*The Ohio State University, William G. Lowrie Department of Chemical and Biomolecular Engineering, Columbus, OH 43210, USA*
[f]*The Ohio State University, Center for Electron Microscopy and Microanalysis (CEMAS), Columbus, OH 43210, USA*
[g]*Juan N. Corpas University Foundation, Center of Phytoimmunomodulation Department of Medicine, Bogota, Colombia*
[h]*The Ohio State University, Department of Materials Science and Engineering, Columbus, OH 43210, USA*
[i]*The Ohio State University, Department of Surgery, Columbus, OH 43210, USA*
[j]*The Ohio State University, Dorothy M. Davis Heart and Lung Research Institute, Columbus, OH 43210, USA*
[k]*The Ohio State University, Department of Neurological Surgery, Columbus, OH, 43210, USA*

† Electronic supplementary information (ESI) available. See DOI: https://doi.org/10.1039/d3bm00573a

suppressor cells (MDSCs) and tumor associated macrophages (TAMs).[4,5] MDSCs are a naturally occurring population of immature myeloid cells with immunosuppressive functions. These cells are abnormally increased in cancer patients and migrate to tumors,[6] where they regulate the function of innate immune effectors and antigen-specific cells.[7] Once MDSCs infiltrate the tumor, they can accumulate as immature cells or transition into mature TAMs. Over time, these tumor-resident myeloid cells are directed by cancer cells to express an anti-inflammatory, alternatively activated (M2-like) phenotype, which hinders anti-tumor immunity.[1,8–11] Hyperproduction of reactive oxygen species, cytokine inhibition, and direct suppression of T cell responses are thought to partially underlie the immunosuppressive effect of tumor-resident myeloid cells. Furthermore, evidence suggests that these are implicated in promoting angiogenesis, which favors tumor progression and metastasis.[12–14] The presence of MDSCs and TAMs has been shown to correlate well with reduced survival in patients with breast and colorectal cancer.[15] As such, approaches that can efficiently target the immune suppressive function of tumor-resident myeloid cells are needed for the development of more effective therapies against cancer.

Repolarization strategies (*e.g.*, pharmacological, genetic, or chemical/biochemical manipulation) that reverse the M2-like phenotype and promote a pro-inflammatory classically activated (M1-like) phenotype in tumor-resident myeloid cells, have emerged as promising tools to restore immune surveillance in the tumor niche.[16–21] The M1-like phenotype has been shown to exhibit anti-tumoral activity *via* the secretion of free radicals (*e.g.*, nitric oxide)[22] and pro-inflammatory/immunostimulatory cytokines such as tumor necrosis factor-α (TNFα), interleukin-1 beta (IL-1β), interleukin-6 (IL-6), and inducible nitric oxide synthase (iNOS), among others.[23] Nevertheless, while promising, current approaches to myeloid cell repolarization for cancer therapies face multiple hurdles, including the need for cumbersome genetic manipulation techniques (*e.g.*, *SIRT1* or *LILRB3* deletion), off-target toxicity/side effects of pharmacological/biochemical agents (*e.g.*, doxorubicin, anti-GR-1 antibodies), and the potential toxicity of certain synthetic chemical compounds (*e.g.*, cationic polymers).[19,24] Therefore, novel myeloid cell repolarization/engineering approaches are needed to stem immunosuppressive functions within the tumor niche.

Non-viral natural carriers offer significant advantages over viral vectors for immunosuppressive cell engineering given their improved safety, reduced immune response, and lower risk of insertional mutagenesis, making them a feasible alternative strategy for repeated administrations.[25,26] Extracellular vesicles (EVs), for example, are cell-derived natural vehicles that play an important role in mediating cellular communication and have emerged as promising non-viral carriers due to their low immunogenicity, stability in biofluids, and ability to cross biological barriers.[27] Previous studies have shown the production of engineered EVs, after the manipulation of donor cells, decorated with ligands for targeted delivery of specific molecular cargo for different applications.[28–30] Additionally, EVs circumvent many of the practical and translational barriers that are characteristic of other delivery systems by offering flexibility in cargo size, unlike viral vectors that have inherent capsid size restrictions,[29] and improved transfection efficiency and low toxicity compared to synthetic carriers.[25] However, EVs derived from progenitor/stem cell populations still face several challenges limiting their clinical translation, such as an increased risk of tumorgenicity, immunogenicity, and limited cell sources.[31] Nevertheless, our group's recent studies suggest that EVs derived from more readily available cell sources, like allogeneic fibroblasts,[28,30] may hold the potential to overcome these obstacles due to their reduced immunogenicity and current use in clinical applications,[30] highlighting them as a promising cell source for EV-based therapeutics.

Here we explored the use of engineered EVs decorated with ICAM-1 ligands to promote preferential retention by myeloid cells within the tumor niche *via* the CD11b/CD18 (Mac-1) receptor–ligand interaction,[32,33] and loaded with microRNA (miRNA) 146a (miR-146a) and *Glut1* mRNA transcripts to drive intratumoral repolarization of myeloid cells towards a more pro-inflammatory phenotype. miR-146a downregulation has been reported to play a role in the development of TAMs, which promote tumor progression and invasion.[34] EV-mediated delivery of *Glut1* mRNA, on the other hand, is expected to drive M1-directed conversions in myeloid cells *via* metabolic reprogramming.[35–38] Therapy deployment was conducted *via* a weekly intratumoral injection of *in vitro*-derived engineered EVs, or through tissue nano-transfection (TNT)-driven engineered EV secretion from the skin that overlaid the tumor.[39] Our results indicate that ICAM-1-decorated EVs loaded with miR-146a and *Glut1* effectively promoted a shift in the myeloid cell compartment of the tumor niche towards a pro-inflammatory state. This was complemented by increased T cell infiltration and reduced tumor and metastatic burden. Altogether, our findings suggest that ICAM-1-decorated engineered EVs could represent a powerful platform nanotechnology for more targeted delivery of genetic cargo to myeloid cells, which could potentially find use in a wide variety of applications beyond cancer (*e.g.*, vaccines). Moreover, the combination of miR-146a and *Glut1* appears to result in an effective cocktail that promotes pro-inflammatory conversions in myeloid cells for applications in immunomodulatory therapies.

## Results and discussion

### Co-transfection of MDSCs with miR-146a and *Glut1* drives a decrease in anti-inflammatory gene expression and an increase in pro-inflammatory gene expression

To evaluate the impact of co-overexpressing miR-146a and *Glut1* on the expression patterns of pro- and anti-inflammatory genes in tumor-associated myeloid cells, cultures of MSC-2, a MDSC murine cell line,[2,6,40,41] were transfected with miR-146a and/or *Glut1* plasmid DNA, and gene expression was evaluated *via* RT-qPCR 7 days post-transfection (Fig. 1A). Cells trans-

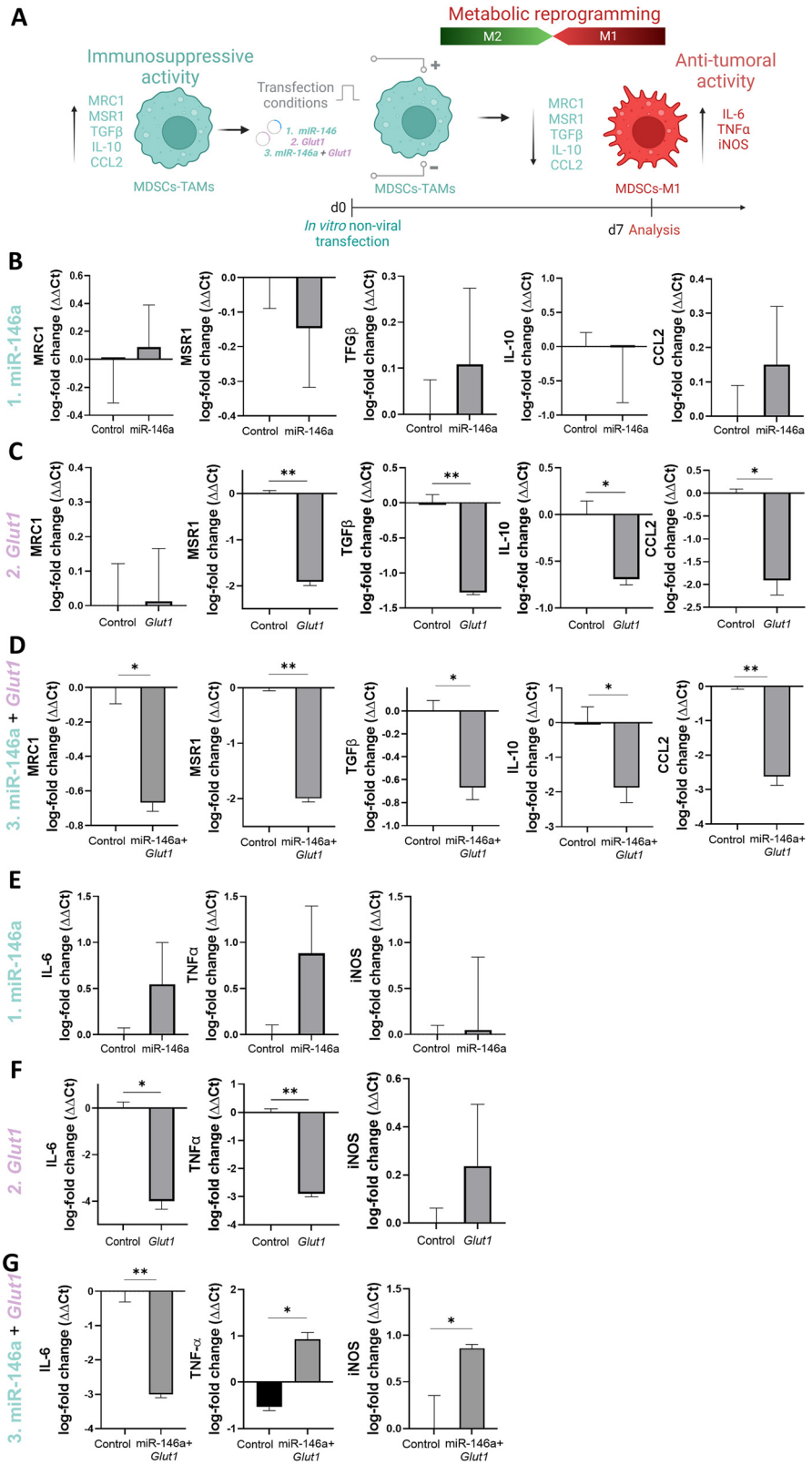


**Fig. 1** Co-transfection with miR-146a and *Glut1* drives pro-inflammatory polarization in MDSCs *in vitro*. (A) Schematic diagram illustrating the *in vitro* transfection of MDSCs at day 0 (d0) with expression plasmids for (1) miR-146a, (2) *Glut1*, or (3) miR-146a + *Glut1*, and the evaluation of the expression patterns at day 7 (d7) of anti- and pro-inflammatory genes. RT-qPCR analyses of (B–D) anti-inflammatory (*MRC1*, *MSR1*, *TGF-β*, *IL-10*, and *CCL2*) and (E–G) pro-inflammatory (*IL-6*, *TNF-a*, *iNOS*) genes. The results show that the combination of miR-146a and *Glut1* leads to downregulation of all the anti-inflammatory genes and upregulation of most of the pro-inflammatory genes. All error bars are shown as standard error of the mean (SEM). *$p < 0.05$ and **$p < 0.001$. Two-tailed *t*-test ($n = 4$).

fected with sham/empty plasmids were used as controls. Previous studies have found that miR-146a is significantly downregulated in TAMs in both, murine models of breast cancer as well as breast cancer patients,[34] which made us hypothesize that miR-146a upregulation could potentially stem M2-directed polarization in MDSCs. We found that direct transfection of miR-146a plasmids into MDSCs did not have any impact in the expression patterns of the anti-inflammatory genes mannose receptor C type-1 (*MRC1*), macrophage scavenger receptor-1 (*MSR1*), transforming growth factor beta (*TGF-β*), interleukin-10 (*IL-10*), and chemokine (C–C motif) ligand 2 (*CCL2*) (Fig. 1B), or pro-inflammatory genes *IL-6*, *TNF-α*, and *iNOS* (Fig. 1E). Direct transfection with *Glut1* plasmids, on the other hand, led to a marked decrease in the expression of anti-inflammatory genes *MSR1*, *TGF-β*, *IL-10*, and *CCL2* (Fig. 1C) seven days post-transfection. However, there was no upregulation of pro-inflammatory genes, as *IL-6* and *TNF-α* expression seemed to be negatively impacted by *Glut1* transfection in MDSCs (Fig. 1F). Notably, when MDSCs were co-transfected with miR-146a and *Glut1* plasmids, we found a more pronounced effect in the expression patterns of pro- and anti-inflammatory genes, with clear downregulation of all anti-inflammatory genes (*MRC1*, *MSR1*, *TGF-β*, *IL-10*, and *CCL2*) (Fig. 1D), accompanied by a marked upregulation of pro-inflammatory genes *TNF-α* and *iNOS* (Fig. 1G) 7 days post transfection.

Next, we sought to identify the mechanisms potentially underlying the shift in gene expression patterns in MDSCs from anti- to pro-inflammatory, in response to the co-overexpression of miR-146a and *Glut1*. First, using 4 different miRNA databases (miRWalk,[42] TargetScan,[43] miRDB,[44] and miRTarBAse[45]), we compiled a list of candidate target mRNAs for miR-146a-5p and miR-146a-3p, the mature miRNAs generated by miR-146a processing. The collected list for each database and a consolidated target mRNA list was created by including those genes present in at least 3 of the 4 databases. Using this strategy, we identified 567 target genes for miR-146a. Functional analysis performed with the Qiagen Ingenuity Pathway Analysis (IPA) software,[37,46] allowed the identification of the main canonical pathways represented in the list of targets and included in the Hematological System Development and Function category. With this approach, we were able to reduce the list of targets to 140 target genes for miR-146a (ESI Fig. 1A, and Table 1†). For *Glut1*, using StringDB database, we found 10 interacting genes using the default stringency parameters (ESI Fig. 1B and Table 2†). Finally, analysis of the main interactions of the *Glut1* together with the IPA results led us to the identification of the hypoxia-inducible factor 1α (HIF1α) as the common canonical pathway shared by miR-146a targets and Glut1 (ESI Fig. 2C†). Based on the results, we hypothesize that the synergistic effect of miR-146a and *Glut1*, by which MDSCs could acquire a pro-inflammatory phenotype, can potentially be mediated by metabolic reprogramming likely driven by an increase of glucose uptake *via Glut1* overexpression.[37,47] Increased glucose uptake, in turn, could lead to an increase in glycolysis and the production of reactive oxygen species (ROS), further contributing to the reprogramming towards a pro-inflammatory phenotype[48] *via* activation of the mitogen-activated protein kinases (MAPK).[49] The activation of these pathways leads to the induction of HIF1α-mediated transcription of genes like *Glut1* [50] and iNOS,[51] an effect responsible for the regulation of MDSC function and differentiation within the tumor microenvironment.[52] miR-146a, in contrast, is able to attenuate the activity of the NF-κB pathway *via* the downregulation of *Irak1* and *Traf*,[53] resulting in the attenuation of the pro-inflammatory phenotype controlled by this pathway (ESI Fig. 2C†). However, miR-146a can also reduce the autoregulatory mechanism induced by the NF-κB pathway, which can also lead to a resolution of inflammatory processes.[54] Since our results indicate that the transfection of miR-146a alone does not have an effect on the expression of pro- or anti-inflammatory genes in MSC2s, we conclude that the synergistic effect of *Glut1* and HIF1α pro-inflammatory program, together with the attenuation of NF-κB pathway mediated by miR-146a, may explain the shift in gene expression that favors pro-inflammatory genes over anti-inflammatory genes observed in myeloid-derived cells within the tumor.

### ICAM-1-decorated EVs show preferential uptake in MDSCs compared to breast cancer cells, and drive a pro-inflammatory shift in MDSCs when loaded with miR-146a and *Glut1* mRNA

Once we defined that co-overexpression of miR-146a and *Glut1* can lead to pro-inflammatory polarization of MDSCs, we set out to develop a method to deliver these factors into MDSCs *via* engineered EVs, which were decorated on the surface with ICAM-1 ligands to promote binding with the CD11b receptor on myeloid cells. Engineered EVs were derived from primary mouse embryonic fibroblast (MEF) cultures co-transfected with expression plasmids for miR-146a, *Glut1*, and *ICAM-1*, following methods previously published by us and others.[28–30,55–57] Control EVs were obtained by transfecting cells with sham/empty plasmids (Fig. 2A). Nanoparticle tracking analyses (NTA) show that at 24 hours after transfection, there is a significant increase in the number of EVs released by engineered cells (*i.e.*, ICAM-1-decorated, loaded with miR-146a and *Glut1* mRNA) compared to control EVs (Fig. 2B and ESI Fig. 3†), with an average particle size ranging between 160 and 260 nm (Fig. 2C and ESI Fig. 3†). RT-qPCR analysis of the EV cargo revealed a significant increase in miR-146a (Fig. 2D) and *Glut1* (Fig. 2E) transcripts compared to control EVs. Moreover, western blot analysis confirmed a marked presence of ICAM-1 in the engineered EVs relative to control EVs (Fig. 2F).

To evaluate if ICAM-1-decorated EVs preferentially interact with myeloid cells, MDSCs were co-cultured with mouse breast cancer cells, PyMT8119, and exposed to fluorescently labeled EVs (Fig. 2G). The results indicate that MDSCs and breast cancer cells uptake control EVs at the same rate (Fig. 2H and I). However, ICAM-1 decoration in the engineered EVs clearly enhanced the uptake rate by the MDSCs (Fig. 2H and I). No significant differences were found in the uptake rate of EVs in breast cancer cells for engineered EVs compared to control EVs

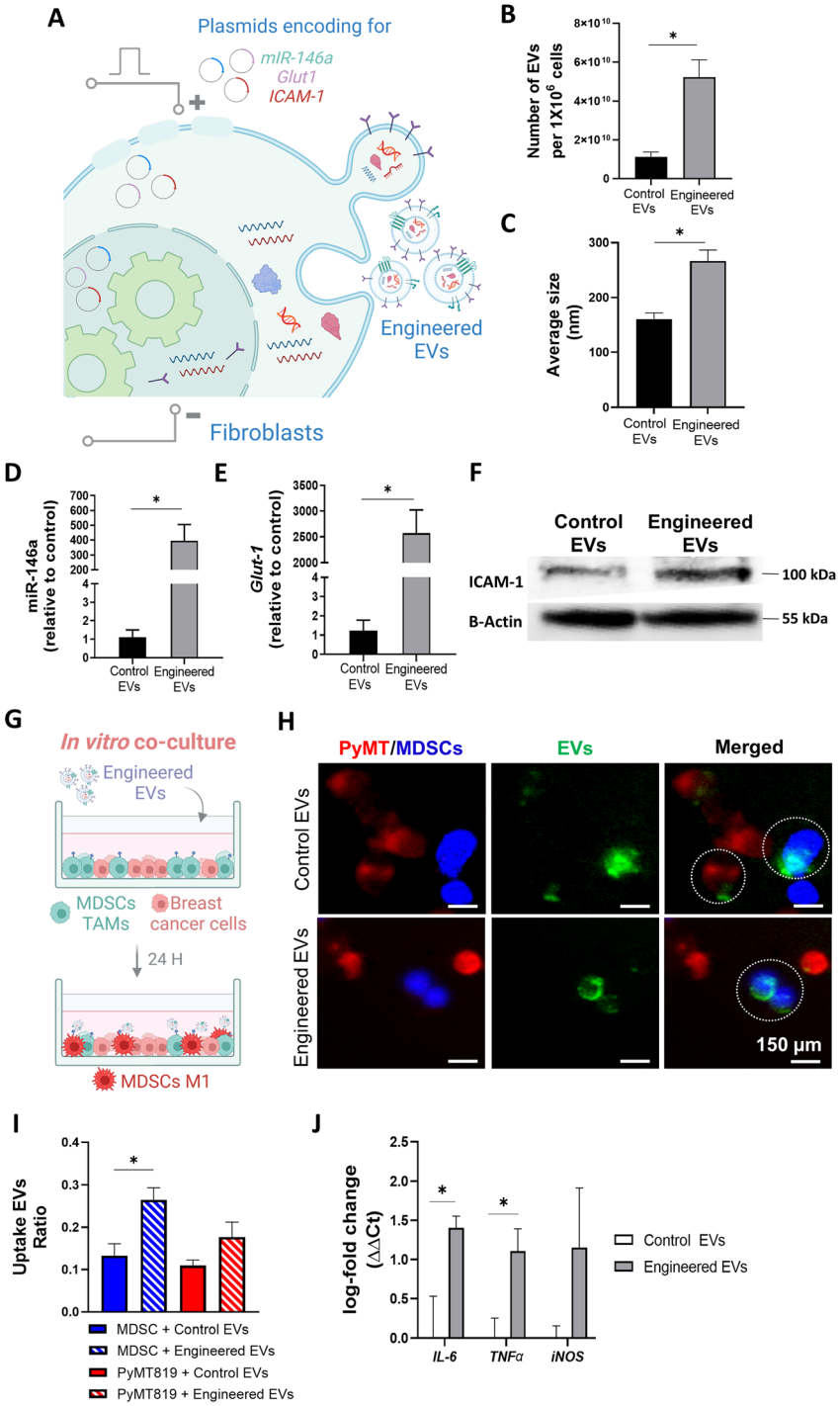


**Fig. 2** Engineered EVs show preferential uptake in MDSCs compared to breast cancer cells and drive a pro-inflammatory shift in MDSCs. (A) Schematic representation of the transfection of mouse fibroblasts with expression plasmids for the molecular cargo (miR-146a and *Glut1*) and targeting ligand (ICAM-1), and the generation of ICAM-1-decorated EVs 24 hours after transfection, loaded with miR-146a and *Glut1* (engineered EVs). (B) NanoSight analysis showing and increase in the number of engineered EVs produced and released by the 'donor' cells compared to control EVs. (C) Engineered EVs show a larger average particle size (~260 nm) compared to control EVs (~160 nm). RT-qPCR analysis showing increased loading of (D) miR-146a and (E) *Glut1* in engineered EVs compared to control EVs. (F) Western blot analysis shows a marked presence of ICAM-1 protein in the engineered EVs compared to control EVs, using β-actin as the internal control. (G) Illustration of the *in vitro* co-culture setting of fluorescently labeled MDSCs (blue) and breast cancer cells (red) treated with engineered or control EVs (green) to evaluate their targeting abilities. (H) Representative micrographs showing EV uptake by the cells. (I) Quantification of EV uptake by the different cells showing that engineered EVs (ICAM-1 decorated EVs loaded with miR-146a + *Glut1*) were internalized at a higher rate by MDSCs compared to control EVs. (J) RT-qPCR analysis of the MDSCs (after magnetic immunoseparation of CD11b+ cells) showing the upregulation of pro-inflammatory markers (*IL-6* and *TNF-a*) when treated with engineered EVs compared to control EVs. All error bars are shown as standard error of the mean (SEM). *$p < 0.05$. One-way ANOVA or two-tailed *t*-test when appropriate ($n = 4–10$).

(Fig. 2H and I). Finally, to evaluate the impact of the miR-146a and *Glut1* mRNA loaded inside EVs on cell responses, MDSC-PyMT8119 co-cultures were exposed to engineered or control EVs, and RT-qPCR was used to evaluate the expression of pro-inflammatory genes in MDSCs following magnetic immunoseparation of $CD11b^+$ cells. Our results show a clear increase in the expression of pro-inflammatory genes *IL-6* and *TNF-a* for co-cultures treated with engineered EVs compared to control EVs (Fig. 2J), thus suggesting that ICAM-1-decorated EVs loaded with miR-146a and *Glut1* mRNA could potentially be used to turn 'cold' tumors 'hot', by driving pro-inflammatory responses in the myeloid cell compartment.[58,59]

### ICAM-1-decorated EVs loaded with miR-146a and *Glut1* mRNA reduce tumor growth and metastatic burden in a murine model of breast cancer

Once we established that ICAM-1 decoration of the EVs promotes preferential interactions with myeloid cells, and that loading with miR-146a and *Glut1* mRNA drives pro-inflammatory gene expression in MDSCs co-cultured with breast cancer cells, we proceeded to evaluate if this EV formulation could be used to treat tumors *in vivo* (Fig. 3A). These experiments were conducted in FBV-MMTV-PyMT (mammary tumor virus-polyoma virus middle T antigen, referred as $PyMT^+$) transgenic mice, which express the oncogene PyMT in epithelial cells of the mammary gland, and are widely used as a pre-clinical model of breast cancer development and metastasis.[60] Breast cancer development in the $PyMT^+$ mice resemble the stages of tumor progression found in human mammary cancer, including hyperplasia, adenoma, early carcinoma, and late invasive carcinomas. Engineered and control EVs were derived from MEF cultures, as previously described. In this case, control EVs were also decorated with ICAM-1, but devoid of miR-146a and *Glut1*. Once the tumors reached a size of ~5 mm, we proceeded to inject $\sim 1 \times 10^9$ engineered or control EVs directly into the tumor site, ensuring that the EVs can primarily act within the tumor microenvironment. Injections were conducted once a week for 5 weeks. Volume measurements at week 5, with respect to the size measured at time 0 (when the treatment was initiated), showed that tumors treated with control EVs had a ~6-fold-increase in volume compared to engineered EVs (Fig. 3B and C), clearly suggesting a role for miR-146a and *Glut1* loading in stemming the progression of tumor growth. Moreover, analysis of lung metastases indicates that mice treated with engineered EVs also showed a significantly reduced metastatic burden compared to mice treated with control EVs (Fig. 3D and E). To evaluate whether the reduction of the tumor and metastatic burden were correlated with phenotypic changes in the immune cell population of the tumor, we proceeded to conduct immunohistological and flow cytometry analyses in tumors harvested from mice treated with engineered EVs or control EVs. Flow cytometry analysis of tumors from mice treated with engineered EVs showed a significant decrease in the number of monocytic MDSCs (*i.e.*, $CD11b^+Ly6C^{hi}Ly6G^{low}$) (Fig. 3F and G), and a marked increase in the number of cytotoxic $CD8^+$ T lymphocytes (Fig. 3H and I), compared to mice treated with control EVs. No differences were noted in the number of CD4 T cells (Fig. 3H and J). Finally, immunostaining analysis revealed a significant expression of the pro-inflammatory marker iNOS in tumors from mice treated with engineered EVs compared to control EVs (Fig. 3K and L). Altogether, these results suggest that tumors treated with ICAM-1-decorated EVs loaded with miR-146a and *Glut1* display a shift in the immune cell population towards a more pro-inflammatory state, presumably favoring enhanced infiltration of cytotoxic T cells.

### Tissue nano-transfection (TNT)-based delivery of *ICAM-1*, miR-146a, and *Glut1* plasmids into the skin surrounding the tumor drives immunomodulation and hinders tumor progression

Previously we reported that TNT can be used to generate engineered EVs from the skin with specific genetic cargo (*e.g.*, reprogramming genes) for downstream applications in regenerative medicine.[39] TNT uses solid-state nanochannels to create small openings and electrophoretically deliver genetic cargo (*e.g.*, plasmid DNA) to cells on the skin surface in a fast, efficient, and benign manner[39] (ESI Fig. 2†). Previously we found that the transcribed genetic cargo (following TNT) can be packed into EVs and relayed to the underlying tissue bed.[39] Here we studied whether TNT can be used to generate (*i.e.*, locally) autologous immunomodulatory EVs from the skin that covers the tumor, as an alternative route of delivery for potential applications in cancer therapies (Fig. 4A). Once the tumors reached a size of ~5 mm, we proceeded to TNT-treat the skin that overlaid the tumor once a week for up to 5 weeks, to maximize the interaction of skin-derived EVs with the tumor microenvironment. Characterization of the skin-derived EVs 24 hours after TNT with treatment (*ICAM-1* + miR-146a + *Glut1* plasmids) or control cocktails (*ICAM-1* + sham/empty plasmids) shows $\sim 10^{11}$ EVs per $cm^2$ TNT-treated skin, with an average size of ~240 nm, as confirmed *via* NTA (ESI Fig. 4A and B†) and cryo-electron microscopy (EM) (Fig. 4B). Western blot analyses also confirmed the presence of ICAM-1 ligands on the TNT-engineered EVs compared to controls (ESI Fig. 4C†). Moreover, RT-qPCR analysis indicate the successful loading of miR-146 and *Glut1* (ESI Fig. 4D and E†) in EVs compared to controls. Analyses of tumor progression indicate that weekly TNT-based delivery of *ICAM-1*, miR-146a, and *Glut1* plasmids into the skin that overlays the tumor results in a marked decrease in tumor growth at week 4 and 5 compared to control tumors, which show a 6-fold increase in size (Fig. 4C and D) with respect to the size measured at time 0. Similar to what we observed with intratumoral delivery of engineered EVs (Fig. 3F–J), the TNT treatment also resulted in significant decrease in tumor resident MDSCs (*i.e.*, CD11b + $Ly6C^{hi}Ly6G^{low}$) (Fig. 4E and F), and a marked increase in $CD8^+$ T lymphocytes (Fig. 4G and H). For these experiments, a marked increase in $CD4^+$ T lymphocytes was also noted (Fig. 4G and I). Finally, immunostaining analysis showed increased immunoreactivity for the pro-inflammatory marker iNOS in mice that were TNT-treated with the treatment cocktail compared to the controls (Fig. 4J and K), which was correlated

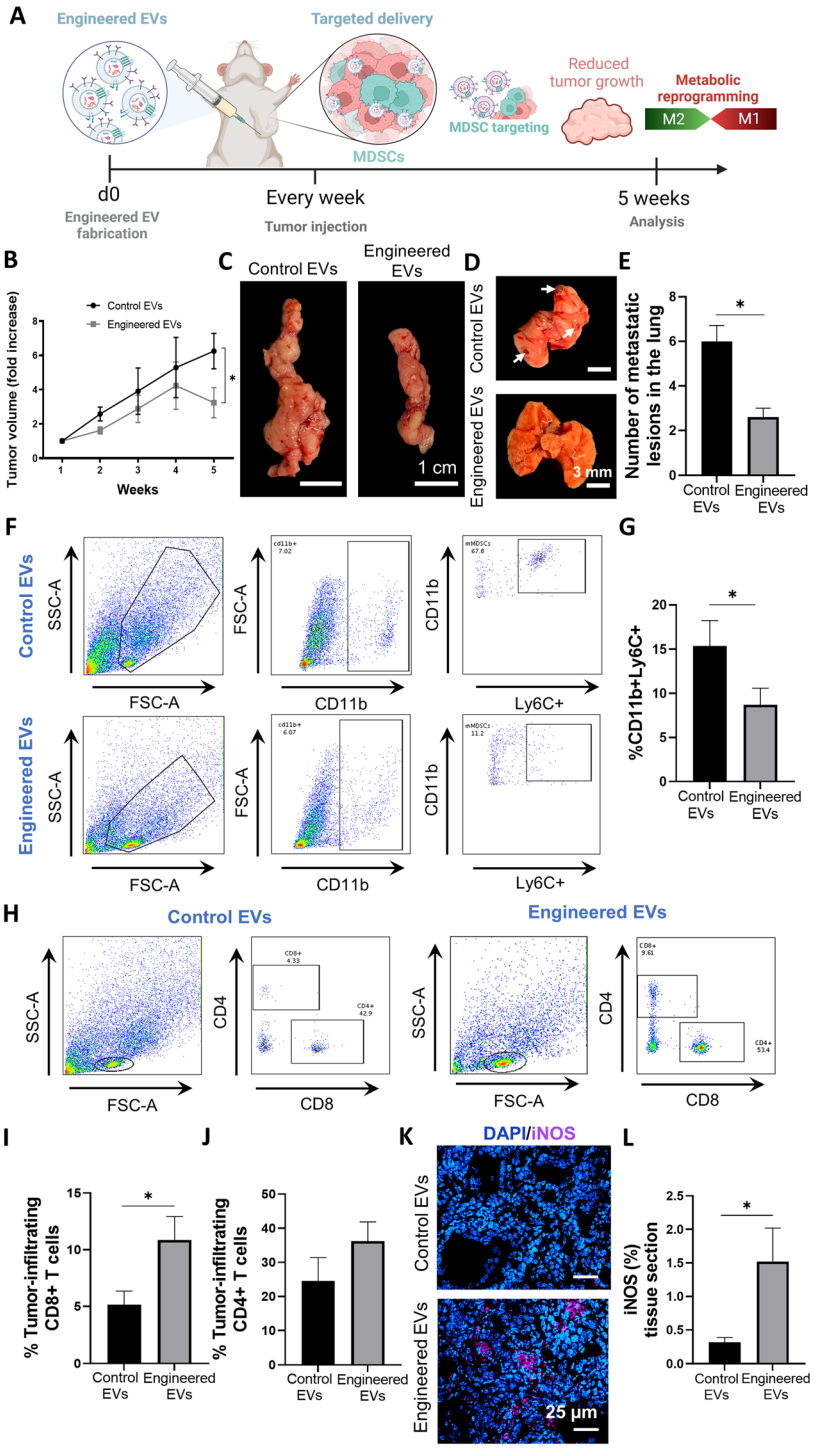


**Fig. 3** ICAM-1-decorated EVs loaded with miR-146a and *Glut1* mRNA reduce tumor growth and metastatic burden in a murine model of breast cancer. (A) Schematic illustration of intratumoral injection of engineered or control EVs, every week for up to 5 weeks, to specifically target myeloid cells within the tumor niche. Tumor length ($l$) and width ($w$) were measured with a caliper and tumor volume was calculated with the formula $w \times l^2/2$. (B) Measurements of the tumor volume recorded every week showing a significant reduction in growth at week 5 when treated with engineered EVs compared to control EVs. (C) Representative pictures of the mammary gland tumor and (D) lung metastases after 5 weeks. (E) Quantification of the number of metastatic nodules present on the surface of the lungs suggests a decrease in metastatic burden for mice treated with engineered EVs compared to control EVs. Flow cytometry analyses of the mammary gland tumors shows a (F and G) decrease in the number of monocytic MDSCs ($CD11b^{+}Ly6C^{hi}Ly6G^{-}$) as well as an increase in the number of (H and I) tumor-infiltrating CD8+ T cells for tumors treated with engineered EVs compared to control EVs. (H and J) No differences were noted in the percentage of tumor-infiltrating CD4+ T cells. (K) Immunofluorescence micrographs of tumor tissue showing the expression of the pro-inflammatory marker iNOS (purple) and the nuclear stain DAPI (blue), with (L) higher percentage of iNOS present in the engineered EV group compared to the control. All error bars are shown as standard error of the mean (SEM). *$p < 0.05$. Two-tailed $t$-test ($n$ = 10–11).

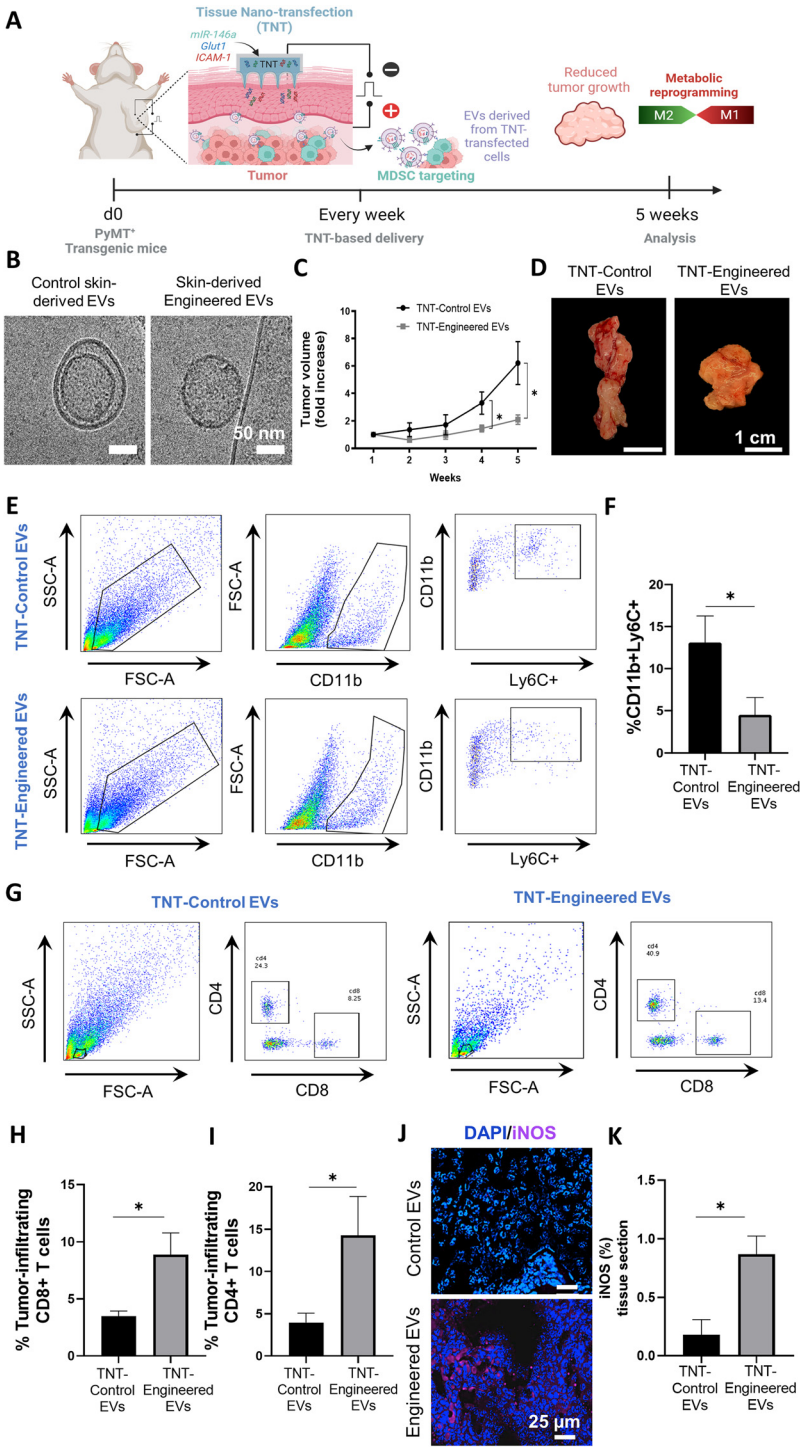


**Fig. 4** Tissue nano-transfection (TNT)-based delivery of miR-146a, *Glut1*, and *ICAM-1* plasmids into the skin surrounding the tumor drives immunomodulation and hinders tumor progression. (A) Schematic diagram depicting the TNT process with plasmids encoding for miR-146a, *Glut1*, and ICAM-1, on the skin surrounding the mammary gland tumor of PyMT+ transgenic mice, and the development of engineered EVs loaded with the molecular cargo and decorated with the ligand ICAM-1. TNT was repeated every week for up to 5 weeks. TNT with *ICAM-1* plasmids was used to produce control EVs. (B) Cryo-EM images of EVs isolated from the skin surrounding the tumors 24 hours after TNT. (C) Measurements of the tumor volume recorded every week for up to 5 weeks showing a significant reduction in growth at week 4 and 5 when treated with TNT-engineered EVs compared to TNT-control EVs. (D) Representative pictures of the mammary gland tumor dissected after 5 weeks. Flow cytometry analyses of the mammary gland tumors shows a (E and F) decrease in the number of monocytic MDSCs ($CD11b^{+}Ly6C^{hi}Ly6G^{-}$) as well as an increase in the number of (G–I) both tumor-infiltrating CD8+ and CD4+ T cells for TNT-engineered EVs compared to TNT-control EVs. (J) Immunofluorescence micrographs of tumor tissue showing the expression of the pro-inflammatory marker iNOS (purple) and the nuclear stain DAPI (blue), with (K) higher percentage of iNOS positive signal in the TNT-engineered EV group compared to the TNT-control EVs. All error bars are shown as standard error of the mean (SEM). *$p < 0.05$. Two-tailed *t*-test ($n = 10–11$).

**Table 1** List of plasmids DNA used in this study

| Plasmid vector | Company | Cat. no | Type | Tag | Vector |
|---|---|---|---|---|---|
| pCMV6-entry tagged cloning vector | Origene | PS100001 | N/A | Myc-DDK | pCMV6-entry |
| ICAM-1-mouse intracellular adhesion molecule-1 | Origene | MG227081 | Mouse Tagged ORF clone | Myc-DDK | pCMV6-entry |
| SLC2a1 mouse solute carrier family 2 (facilitated glucose transporter | Origene | MR207871 | Mouse Tagged ORF clone | Myc-DDK | pCMV6-entry |
| miR-146a mouse MicroRNA expression plasmid | Origene | SC400782 | N/A | N/A | pCMV-MIR |

**Table 2** List of primers used in gene expression analysis

| Gene symbol | Gene name | Gene aliases | Company | Cat. no. |
|---|---|---|---|---|
| TNF-α | Tumor necrosis factor | DIF, TNF-a, TNF-alpha | Thermofisher Scientific | Mm00443258_m1 |
| IL-6 | Interleukin 6 | IL-6 | Thermofisher Scientific | Mm00446190_m1 |
| NOS2 | Nitric oxide synthase 2, inducible | NOS-II, Nos-2, Nos2a, i-NOS, iNOS | Thermofisher Scientific | Mm00440502_m1 |
| IFN-β | Interferon beta 1, fibroblast | IFN-beta, IFNB, Ifb | Thermofisher Scientific | Mm00439552_s1 |
| IL-27 | Interleukin 27 | IL-27, IL-27p28, Il30, p28 | Thermofisher Scientific | Mm00461162_m1 |
| Slc2a1 | Solute carrier family 2 (facilitated glucose transporter), member 1 | *Glut1*, Glut1 | Thermofisher Scientific | Mm00441480_m1 |
| MRC1 | Mannose receptor, C type1 | AW259686, CD206, MR | Thermofisher Scientific | Mm01329362_m1 |
| MSR1 | Macrophage scavenger receptor 1 | MRS-A, MSR, MSR-A, SR-AI, SR-AII, Scara1, Scvr | Thermofisher Scientific | Mm00446214_m1 |
| TGFβ | Transforming growth factor, beta 1 | TGF-beta1, TGFbeta1, Tgfb, Tgfb-1 | Thermofisher Scientific | Mm01178820_m1 |
| IL-10 | Interleukin 10 | CSIF, Il-10 | Thermofisher Scientific | Mm01288386_m1 |
| CCL-2 | Chemokine (C–C motif) ligand 2 | MCP-1, MCP1, SMC-CF, Scya2, Sigje | Thermofisher Scientific | Mm00441242_m |
| miR-146a | mmu-miR-146a-5p | N/A | Thermofisher Scientific | Mmu478399_mir |
| 18S | Eukaryotic 18S rRNA | N/A | Thermofisher Scientific | Hs99999901_s1 |
| GAPDH | Glyceraldehyde-3-phosphate dehydrogenase | Gapd | Thermofisher Scientific | Mm99999915_g1 |

**Table 3** List of flow cytometry antibodies used in this study

| Antibody | Clone | Type | Catalog no. | Application | Company |
|---|---|---|---|---|---|
| CD8-FITC | 53-6.7 | Monoclonal | 100706 | FC | Biolegend |
| CD4-APC | GK1.5 | Monoclonal | 100412 | FC | Biolegend |
| CD11b-pacific blue | M1/70 | Monoclonal | 101224 | FC | Biolegend |
| F4/80-FITC | BM8 | Monoclonal | 123108 | FC | Biolegend |
| CD80-PercP | 16-10A1 | Monoclonal | 104722 | FC | Biolegend |
| CD206-APC | C068C2 | Monoclonal | 141708 | FC | Biolegend |
| CD11b-FITC | M1/70 | Monoclonal | 10120 | FC | Biolegend |
| Ly6-G-PE | 1A8 | Monoclonal | 127608 | FC | Biolegend |
| Ly6-C-APC | HK1.4 | Monoclonal | 128016 | FC | Biolegend |

**Table 4** List of antibodies for immunofluorescence used for this study

| Target primary | Primary antibody | Raised | Cat. no. | Company | Conc. | Secondary antibody | Conc. |
|---|---|---|---|---|---|---|---|
| M1 macrophages | iNOS | Rabbit | ab178945 | Abcam | 1 : 500 | Goat pAB to rabbit IgG Cy5 (647) (H + L) | 1 : 200 |
| M1 macrophages | CD68 | Rat | ab53444 | Abcam | 1 : 100 | Goat pAb to rat IgG Cy5 (568) (H + L) | 1 : 200 |
| TIMP-3 | TIMP-3 | Rabbit | Ab39184 | Abcam | 1 : 250 | Goat pAB to rabbit IgG 488 (H + L) | 1 : 200 |
| Cytotoxic T cells | CD8 | Rat | ab22378 | Abcam | 1 : 100 | Goat pAb to rat IgG Cy5 (650) (H + L) | 1 : 200 |

in more than 70% of the cases with classically activated macrophages (ESI Fig. 5†). Altogether, these results suggest that TNT-based treatment of the skin that covers the tumor results in the generation of immunomodulatory EVs, locally, which are presumably driving pro-inflammatory changes in the immune cell compartment of the tumor niche, thus facilitating the infiltration of cytotoxic effector cells that can hinder tumor growth.

## Conclusions

We developed a novel platform nanotechnology based on ICAM-1-decorated EVs to drive more targeted interactions with myeloid cells as a potential therapeutic approach for cancer. Myeloid cell infiltration into solid tumors has been linked to a decrease in immunosurveillance and enhanced tumor progression. As such, myeloid cell-targeting therapies have

 

emerged as promising adjunctive measures to reactivate immunosurveillance in the tumor niche and enable the development and implementation of more effective anti-cancer treatment regimens. However, while promising, current myeloid cell repolarization approaches face many hurdles. Recent studies on MDSC repolarization with cationic polymers reported therapeutic efficacy with intratumoral injections being conducted every two days.[16] In contrast, our results indicate that a single non-viral co-transfection with miR-146a and *Glut1* can promote pro-inflammatory gene expression patterns in MDSCs. Moreover, loading miR-146a and *Glut1* into ICAM-1-decorated EVs enabled more targeted delivery of repolarizing cargo into myeloid cells, as confirmed in *in vitro* co-cultures of MDSCs and cancer cells. Therapy deployment in a murine model of breast cancer confirmed that a weekly intratumoral injection of allogeneic ICAM-1-decorated EVs loaded with miR-146a and *Glut1* also promoted *in vivo* repolarization of the immune cell compartment toward a more pro-inflammatory phenotype, which presumably resulted in reduced tumor progression and metastatic burden. Moreover, our results show that a weekly TNT-based treatment of the skin that overlays the tumor, aimed at locally repurposing the skin tissue for the production of autologous ICAM-1-decorated EVs loaded with miR-146a and *Glut1* mRNA, also effectively repolarized the immune cell compartment of the tumor and stemmed tumor progression. While our EV deployment strategies were aimed to primarily target the tumor site, future studies should also look into the potential role of engineered immunomodulatory EVs in the surrounding lymph nodes. Altogether, our data indicate that ICAM-1-decorated EVs loaded with miR-146a and *Glut1* could be a viable tool to reactivate immunosurveillance in the tumor niche. Moreover, ICAM-1-decorated EVs could potentially become a powerful platform technology to deploy a myriad of therapeutic cargo to myeloid cells for a wide variety of applications beyond cancer.

# Methods

### Animal husbandry

FVB/N-Tg-mouse mammary tumor virus-polyoma virus T antigen (MMTV-PyVT)-634Mul/J (referred hereafter as $PyMT^+$) and wild-type FVB mice (referred hereafter as $PyMT^-$) were obtained from Jackson Laboratory (Ban Harbor, ME). $PyMT^+$ males were mated with $PyMT^-$ females to generate $PyMT^+$ females and offspring was genotyped according to Jackson Laboratory's protocols, as previously described.[61] All experiments were performed following procedures previously approved by the Animal Care and Use Committee at The Ohio State University (IACUC # 2016A00000074-R2).

### MDSC electroporation

A list of plasmids used for these experiments can be found in Table 1. All plasmids were prepared using a plasmid DNA isolation kit (ZymoPure, cat. no. D4201) following manufacturer's protocol. DNA concentrations were obtained from Nanodrop 2000c Spectrophotometer (ThermoFisher Scientific). MSC-2 cells, a MDSC murine cell line, were transfected with plasmid DNA encoding for miR-146a and/or *Glut1*. MSC-2 cells transfected with sham/empty plasmids (pCMV6) were used as controls. A Neon Transfection System (Thermo Fisher Scientific) was used to carry out the non-viral transfection with 1425 V, 1 pulse, and 30 ms conditions, using a concentration of 0.05 μg per μL per plasmid and a 1 : 1 ratio for the combination cocktail (miR-146a + *Glut1*). Transfection efficiency of the donor cells was evaluated *via* RT-qPCR.

### Bioinformatics

miR-146a (NCBI GeneID: 387164) targets were obtained from the databases miRWalk,[42] TargetScan,[43] miRDB,[44] and miRTarBAse[45] using the two mature miRNAs mmu-miR146-5p (NCBI GeneID: 387164) and mmu-miR-146a-3p as queries. Results from each mature miRNA query were compiled and duplicated genes were consolidated into a single list using RStudio. Finally, a single list of mRNA targets was generated, including targets present in at least 3 of the 4 databases (ESI Table 1†). Analysis of Gene Ontology and Pathways enriched in the generated list was obtained with the Qiagen Ingenuity Pathway Analysis (IPA) software.[46] The identification of Glut1 main interaction was obtained from String DB[62] (ESI Table 2†).

### Manufacturing, characterization, and intratumoral delivery of allogeneic EVs

MEFs (Millapore Sigma, ref. no. PMEF-HL) were transfected with the plasmid combination by electroporation as described before. EVs were isolated from culture media 24 hours post transfection using an exosome isolation kit (ThermoFisher Scientific cat. no. 4478359) following the manufacturer's protocol. EV pellets were stored at −80 °C for subsequent use. NTA was performed using a Nanosight system Malvern NS300. Efficiency of transfection in the cells and EV loading was evaluated by RT-qPCR. PYMT female mice with a palpable tumor (~5 mm in size) were injected with $\sim 1 \times 10^9$ EVs weekly for 5 weeks. Mammary glands were collected and snap frozen or fixed or used immediately for flow cytometry or analytical studies.

### Tissue nano-transfection (TNT)

TNT devices were fabricated as described previously[39,63,64] but with a few modifications.[65] Briefly, nanoscale holes were patterned on a ~1 μm thick layer of S1813 photoresist (PR) spin coated on HMDS-primed wafers using projection lithography and developed using MF-319. Nanoscale channels were then etched into the silicon by deep reactive ion etching (DRIE) (100 cycles, ~10–15 μm depth, 10 s etch using SF6, 5 s deposition using C4F8), and the photoresist was stripped using acetone and sonication. Next, microscale channels/reservoirs (~50 μm diameter) were patterned on the back side of the wafer using a contact aligner and Az12XT resist (~9 mm) and developed using CD-26 developer. This was followed by DRIE (300 cycles, ~185–190 μm depth, 10 s etch using SF6, 5 s depo-

sition using C4F8) until the nanochannels were exposed and subsequent stripping of the resist using acetone and sonication. Finally, to fabricate the needles, microscale pillars were patterned on the nanochannel side using S1813 PR and the contact aligner. The needle pattern was then defined on the nanochanneled silicon surface *via* etching with SF6 (100 sccm for 2.5 min), using the S1813 pattern as an etch mask (ESI Fig. 2†).

The wafers were then diced into ~1 $cm^2$ TNT devices, and plasmid reservoirs were created for each device by affixing a plastic ring to the backside of the silicon. PYMT female mice with palpable tumors (~5 mm in size) were TNT-treated weekly on the skin that overlaid the tumor for 5 weeks. For EV characterization, EVs were isolated directly from the skin that overlays the tumors using a 12 mm-diameter punch. The collected tissue was minced into ~1 mm pieces with a surgical scalpel and dissociated using the multi tissue dissociation kit 1 (Miltenyi Biotec #130-110-201) in combination with the gentleMACS Octo Dissociator (Miltenyi Biotec cat. no. 130-096-427). The resulting supernatant was then removed and EVs were isolated by tangential flow filtration as described before.[66]

### Western blotting analysis

For total protein isolation pelleted EVs were resuspended in lysis buffer containing RIPPA buffer (ThermoFisher Scientific, cat. no. 89900), phosphatase (Sigma-Aldrich, cat. no. P5726-1), and protease (Roche, cat. no. 4693116001) inhibitor cocktails, and 1 mM phenylmethylsufonyl fluoride (PMSF). EVs were incubated for 1 hour under continuous vortex at 4 °C. Isolated proteins were denatured and reduced at 95 °C for 5 min using NuPAGE LDS sample buffer (4×) (ThermoFisher Scientific, cat. no. NP0004) and NuPAGE reducing agent (10×) (ThermoFisher Scientific, cat. no. and NP0007). Then, the samples were loaded and separated using Novex 4–12% bis–tris gels (ThermoFisher Scientific, cat. no. NP000102) for 50 min at 200 V. Subsequently, gels were transferred onto nitrocellulose membranes (ThermoFisher Scientific, cat. no. LC2001). Membranes were blocked with 5% BSA (Sigma-Aldrich, cat. no. 10735094001) for 1 hour at room temperature in 1× Tris buffered saline (TBS) and 0.1% Tween-20 (GE Healthcare, Piscataway NJ) (TBS-T). The primary antibodies ICAM-1 (Santa Cruz Biotechnology, cat. no. SC8439) and β-acting (Cell signaling, cat. no. 4967) were diluted in TBS-T. Finally, the membranes were visualized using a chemiluminescent substrate (Thermo Scientific, cat. no. 34095) following manufacturer's instructions.

### Cryo-electron microscopy (CryoEM)

A total of 3 μL EVs were purified using the protocol described by Zhang *et al.*[66] Purified EVs were applied to a glow discharged lacey carbon coated copper grid (300 mesh, Ted Pella) and flash-frozen in liquid ethane using an automated vitrification device (ThermoFisher Scientific Vitrobot Mark IV). The sample was then visualized in a Glacios Cryo-TEM (ThermoFisher Scientific).

### Gene expression

Total RNA was extracted using trizol reagent (Thermoscientific Scientific, cat. no 15596026). Reverse transcription reaction was performed using SuperScript™ IV VILO™ Master Mix (Thermofisher Scientific, cat. no. 11756500) with 1000–2500 ng of RNA in 20 μL. RT-qPCR was performed using fluorogenic Taqman primers (Thermofisher Scientific) with the following conditions: 95 °C 10 min, 40 cycles of 95 °C 1 min, 60 °C 1 min, and 72 °C 1 min in the QuantStudio 3 real-time PCR system (Thermofisher Scientific). Mouse GAPDH was used as a reference gene in all RT-qPCR reactions. Specific Taqman primers used in PCR reactions are listed in Table 2. Gene expression analysis was performed as previously described by Konigshoff *et al.*[67] Relative gene expression (ΔCt) was determined for each sample as $\Delta Ct = Ct_{reference} - Ct_{target}$. Subsequently, relative gene expression compared to controls (ΔΔCt) was determined for each sample as $\Delta\Delta Ct = \Delta Ct_{treatment} - \text{average}(\Delta Ct_{control})$. ΔΔCt values equate to approximately the logarithm of the fold change. Comparisons between groups were performed using one-tailed *t*-tests.

### Flow cytometry

Mammary tumors were collected aseptically at necropsy and minced with a sterile blade. Briefly, mammary tumors were cut into small pieces, (1–3 mm) and transferred into C tubes (Miltenyi Biotec, cat. no. 130-096-334). To produce a single-cell suspension suitable for FACS analysis, tumor dissociation kit (Miltengyi Biotec, cat. no. 130-096-730) in combination with the "gentleMACS Octo Dissociator" (Miltenyi Biotec cat. no. 130-096-427) were used following the procedure described by the manufacturer. The cell suspension was passed through a cell strainer (70 μM; Miltenyi Biotec, cat. no. 130-098-462) just prior to incubation with fluorescent markers for FACS analysis. $1 \times 10^6$ cells per 100 μL were stained with primary antibodies following the manufacturer's instructions for concentration and incubation times. All samples were acquired with a LSRII flow cytometer (BD Pharmagen) and analyzed with FlowJo software (Ashland, OR). After the exclusion of doublets and debris, tumor associated monocytic MDSCs were gated out based on the expression of CD11b and Ly6C and their absence of Ly6G. CD8+ T and CD4+ T cells were identified by the surface expression of CD8 and CD4 antibodies after the exclusion of dead cells and debris. Fluorochrome-conjugated antibodies are described in Table 3. All antibodies were tested with their respective isotype controls.

### Immunostaining

Mammary tumors were harvested and frozen at −80 °C in OCT (Thermofisher Scientific, cat. no. 4585). OCT embedded mammary tumors were sectioned at 10 μm and mounted to charged microscope slides. Tissue sections were fixed in cold methanol, blocked with 10% normal goat serum and/or mouse on mouse (M.O.M.) blocking reagent, and incubated with specific primary antibodies and subsequent fluorescence-

 

tagged secondary antibodies to visualize target signal. Stained cells and tissue sections were imaged using Nikon TI2-E microscope operating on NIS-Elements AR v5.3. Finally, co-localization analysis was performed using a custom-made script in the Nikon-software NIS elements 5.3, that quantified the positive area ($\mu m^2$) of the Tx-Red channel associated to the CD68 (macrophage marker), the Far-Red channel associated with the iNOS expression, and the double positive area. The percentage of iNOS double positive (%) was then calculated based on the iNOS area and the double positive area. A full list of antibodies used can be found in Table 4.

### Statistical analysis

All data are reported as the mean and standard error. Statistical analyses were completed using GraphPad prism v8. Comparisons between groups were performed using two tail *t*-tests and one-way ANOVA. Statistical outliers (>3 studentized standard deviations) were excluded from respective analyses.

## Author contributions

D. G.-P., S. D.-S. and N. H.-C. conceived the idea and designed the study in collaboration with WEC. The experimental work and characterization were conducted by S. D.-S., A. S.-P., A. P., D. D., C. F., L. O.-P., L. L., K. D., S. S., M. A. R.-B., W. L., N. O., and S. W. Bioinformatics analyses were conducted by D. A.-C. and S. D.-S. Electron microscopy characterization was conducted by B. D. and D. W. M. with support from J. Z., E. R., and A. F. P. The manuscript was prepared by D. G.-P. with support from A. S.-P., S. D.-S. and N. H.-C., with feedback from all co-authors.

## Conflicts of interest

The authors declare no competing financial interests.

## Acknowledgements

Funding for this work was partly provided by a New Innovator Award to DGP NIBIB/NIH (DP2EB028110). We also would like to thank Anthony Vetter from Nikon for his guidance with image analysis. All illustrations were created using BioRender.

## References

1 P. Sharma, S. Hu-Lieskovan, J. A. Wargo and A. Ribas, Primary, Adaptive, and Acquired Resistance to Cancer Immunotherapy, *Cell*, 2017, **168**(4), 707–723.
2 V. C. Shukla, *et al.*, Reciprocal Signaling between Myeloid Derived Suppressor and Tumor Cells Enhances Cellular Motility and is Mediated by Structural Cues in the Microenvironment, *Adv. Biosyst.*, 2020, **4**(6), e2000049.
3 G. A. Rabinovich, D. Gabrilovich and E. M. Sotomayor, Immunosuppressive strategies that are mediated by tumor cells, *Annu. Rev. Immunol.*, 2007, **25**, 267–296.
4 D. I. Gabrilovich, S. Ostrand-Rosenberg and V. Bronte, Coordinated regulation of myeloid cells by tumours, *Nat. Rev. Immunol.*, 2012, **12**(4), 253–268.
5 A. Kano, Tumor cell secretion of soluble factor(s) for specific immunosuppression, *Sci. Rep.*, 2015, **5**, 8913.
6 S. Duarte-Sanmiguel, *et al.*, Guided migration analyses at the single-clone level uncover cellular targets of interest in tumor-associated myeloid-derived suppressor cell populations, *Sci. Rep.*, 2020, **10**(1), 1–8.
7 D. I. Gabrilovich and S. Nagaraj, Myeloid-derived suppressor cells as regulators of the immune system, *Nat. Rev. Immunol.*, 2009, **9**(3), 162–174.
8 V. Kumar, S. Patel, E. Tcyganov and D. I. Gabrilovich, The Nature of Myeloid-Derived Suppressor Cells in the Tumor Microenvironment, *Trends Immunol.*, 2016, **37**(3), 208–220.
9 P. Allavena, A. Sica, C. Garlanda and A. Mantovani, The Yin-Yang of tumor-associated macrophages in neoplastic progression and immune surveillance, *Immunol. Rev.*, 2008, **222**, 155–161.
10 R. Noy and J. W. Pollard, Tumor-associated macrophages: from mechanisms to therapy, *Immunity*, 2014, **41**(1), 49–61.
11 D. M. Kuang, *et al.*, Activated monocytes in peritumoral stroma of hepatocellular carcinoma foster immune privilege and disease progression through PD-L1, *J. Exp. Med.*, 2009, **206**(6), 1327–1337.
12 L. Yang, *et al.*, Expansion of myeloid immune suppressor Gr+CD11b+ cells in tumor-bearing host directly promotes tumor angiogenesis, *Cancer Cell*, 2004, **6**(4), 409–421.
13 R. S. Kerbel, Tumor angiogenesis: past, present and the near future, *Carcinogenesis*, 2000, **21**(3), 505–515.
14 A. Y. Chan, *et al.*, EGF stimulates an increase in actin nucleation and filament number at the leading edge of the lamellipod in mammary adenocarcinoma cells, *J. Cell Sci.*, 1998, **111**(Pt 2), 199–211.
15 S. Solito, *et al.*, A human promyelocytic-like population is responsible for the immune suppression mediated by myeloid-derived suppressor cells, *Blood*, 2011, **118**(8), 2254–2265.
16 W. He, *et al.*, Re-polarizing Myeloid-derived Suppressor Cells (MDSCs) with Cationic Polymers for Cancer Immunotherapy, *Sci. Rep.*, 2016, **6**, 24506.
17 K. N. Kodumudi, *et al.*, A novel chemoimmunomodulating property of docetaxel: suppression of myeloid-derived suppressor cells in tumor bearers, *Clin. Cancer Res.*, 2010, **16**(18), 4583–4594.
18 G. Ma, *et al.*, Paired immunoglobin-like receptor-B regulates the suppressive function and fate of myeloid-derived suppressor cells, *Immunity*, 2011, **34**(3), 385–395.
19 G. Liu, *et al.*, SIRT1 limits the function and fate of myeloid-derived suppressor cells in tumors by orchestrating HIF-1α–dependent glycolysis, *Cancer Res.*, 2014, **74**(3), 727–737.
20 D. Alizadeh, *et al.*, Doxorubicin eliminates myeloid-derived suppressor cells and enhances the efficacy of adoptive

T-cell transfer in breast cancer, *Cancer Res.*, 2014, **74**(1), 104–118.
21 W. C. Yang, G. Ma, S. H. Chen and P. Y. Pan, Polarization and reprogramming of myeloid-derived suppressor cells, *J. Mol. Cell Biol.*, 2013, **5**(3), 207–209.
22 K. Kashfi, J. Kannikal and N. Nath, Macrophage Reprogramming and Cancer Therapeutics: Role of iNOS-Derived NO, *Cells*, 2021, **10**(11), 3194.
23 N. B. Hao, *et al.*, Macrophages in tumor microenvironments and the progression of tumors, *Clin. Dev. Immunol.*, 2012, **2012**, 948098.
24 H. Lv, S. Zhang, B. Wang, S. Cui and J. Yan, Toxicity of cationic lipids and cationic polymers in gene delivery, *J. Controlled Release*, 2006, **114**(1), 100–109.
25 B. Gantenbein, *et al.*, Non-viral Gene Delivery Methods for Bone and Joints, *Front. Bioeng. Biotechnol.*, 2020, **8**(1320), 1–33.
26 M. Ramamoorth and A. Narvekar, Non viral vectors in gene therapy- an overview, *J. Clin. Diagn. Res.*, 2015, **9**(1), Ge01–Ge06.
27 M. Yáñez-Mó, *et al.*, Biological properties of extracellular vesicles and their physiological functions, *J. Extracell. Vesicles*, 2015, **4**, 27066.
28 M. A. Rincon-Benavides, *et al.*, Engineered Vasculogenic Extracellular Vesicles Drive Nonviral Direct Conversions of Human Dermal Fibroblasts into Induced Endothelial Cells and Improve Wound Closure, *Adv. Ther.*, 2022, **6**(3), 2200197.
29 L. Ortega-Pineda, *et al.*, Designer Extracellular Vesicles Modulate Pro-Neuronal Cell Responses and Improve Intracranial Retention, *Adv. Healthcare Mater.*, 2022, e2100805.
30 A. I. Salazar-Puerta, *et al.*, Engineered Extracellular Vesicles Derived from Dermal Fibroblasts Attenuate Inflammation in a Murine Model of Acute Lung Injury, *Adv. Mater.*, 2023, **35**(28), 2210579.
31 A. S. Lee, C. Tang, M. S. Rao, I. L. Weissman and J. C. Wu, Tumorigenicity as a clinical hurdle for pluripotent stem cell therapies, *Nat. Med.*, 2013, **19**(8), 998–1004.
32 G.-O. Ahn and J. M. Brown, Matrix metalloproteinase-9 is required for tumor vasculogenesis but not for angiogenesis: role of bone marrow-derived myelomonocytic cells, *Cancer Cell*, 2008, **13**(3), 193–205.
33 G.-O. Ahn, *et al.*, Inhibition of Mac-1 (CD11b/CD18) enhances tumor response to radiation by reducing myeloid cell recruitment, *Proc. Natl. Acad. Sci. U. S. A.*, 2010, **107**(18), 8363–8368.
34 Y. Li, *et al.*, Functions of miR-146a and miR-222 in Tumor-associated Macrophages in Breast Cancer, *Sci. Rep.*, 2015, **5**, 18648.
35 A. J. Freemerman, *et al.*, Metabolic reprogramming of macrophages: glucose transporter (GLUT1)-mediated glucose metabolism drives a pro-inflammatory phenotype, *J. Biol. Chem.*, 2014, **M113**, 522037.
36 B. Kelly and L. A. O'neill, Metabolic reprogramming in macrophages and dendritic cells in innate immunity, *Cell Res.*, 2015, **25**(7), 771–784.
37 A. J. Freemerman, *et al.*, Myeloid Slc2a1-deficient murine model revealed macrophage activation and metabolic phenotype are fueled by GLUT1, *J. Immunol.*, 2019, **202**(4), 1265–1286.
38 R. Stienstra, R. T. Netea-Maier, N. P. Riksen, L. A. Joosten and M. G. Netea, Specific and complex reprogramming of cellular metabolism in myeloid cells during innate immune responses, *Cell Metab.*, 2017, **26**(1), 142–156.
39 D. Gallego-Perez, *et al.*, Topical tissue nano-transfection mediates non-viral stroma reprogramming and rescue, *Nat. Nanotechnol.*, 2017, **12**(10), 974.
40 A. Stiff, *et al.*, Myeloid-derived suppressor cells express Bruton's tyrosine kinase and can be depleted in tumor-bearing hosts by ibrutinib treatment, *Cancer Res.*, 2016, **76**(8), 2125–2136.
41 P. Trikha, *et al.*, Targeting myeloid-derived suppressor cells using a novel adenosine monophosphate-activated protein kinase (AMPK) activator, *OncoImmunology*, 2016, **5**(9), e1214787.
42 H. Dweep and N. Gretz, miRWalk2.0: a comprehensive atlas of microRNA-target interactions, *Nat. Methods*, 2015, **12**(8), 697.
43 V. Agarwal, G. W. Bell, J. W. Nam and D. P. Bartel, Predicting effective microRNA target sites in mammalian mRNAs, *eLife*, 2015, 4.
44 Y. Chen and X. Wang, miRDB: an online database for prediction of functional microRNA targets, *Nucleic Acids Res.*, 2020, **48**(D1), D127–D131.
45 C. H. Chou, *et al.*, miRTarBase update 2018: a resource for experimentally validated microRNA-target interactions, *Nucleic Acids Res.*, 2018, **46**(D1), D296–D302.
46 A. Krämer, J. Green, J. Pollard Jr. and S. Tugendreich, Causal analysis approaches in Ingenuity Pathway Analysis, *Bioinformatics*, 2014, **30**(4), 523–530.
47 A. J. Freemerman, *et al.*, Metabolic reprogramming of macrophages: glucose transporter 1 (GLUT1)-mediated glucose metabolism drives a proinflammatory phenotype, *J. Biol. Chem.*, 2014, **289**(11), 7884–7896.
48 M. A. Chelombitko, A. V. Fedorov, O. P. Ilyinskaya, R. A. Zinovkin and B. V. Chernyak, Role of Reactive Oxygen Species in Mast Cell Degranulation, *Biochemistry*, 2016, **81**(12), 1564–1577.
49 Y. Son, S. Kim, H. T. Chung and H. O. Pae, Reactive oxygen species in the activation of MAP kinases, *Methods Enzymol.*, 2013, **528**, 27–48.
50 C. Chen, N. Pore, A. Behrooz, F. Ismail-Beigi and A. Maity, Regulation of glut1 mRNA by hypoxia-inducible factor-1. Interaction between H-ras and hypoxia, *J. Biol. Chem.*, 2001, **276**(12), 9519–9525.
51 N. Takeda, *et al.*, Differential activation and antagonistic function of HIF-{alpha} isoforms in macrophages are essential for NO homeostasis, *Genes Dev.*, 2010, **24**(5), 491–501.
52 C. A. Corzo, *et al.*, HIF-1α regulates function and differentiation of myeloid-derived suppressor cells in the tumor microenvironment, *J. Exp. Med.*, 2010, **207**(11), 2439–2453.

 

53 R. Saba, D. L. Sorensen and S. A. Booth, MicroRNA-146a: A Dominant, Negative Regulator of the Innate Immune Response, *Front. Immunol.*, 2014, **5**, 578.
54 T. Lawrence and C. Fong, The resolution of inflammation: anti-inflammatory roles for NF-kappaB, *Int. J. Biochem. Cell Biol.*, 2010, **42**(4), 519–523.
55 S. Duarte-Sanmiguel, *et al.*, In Situ Deployment of Engineered Extracellular Vesicles into the Tumor Niche via Myeloid-Derived Suppressor Cells, *Adv. Healthcare Mater.*, 2022, **11**(5), 2101619.
56 S. Duarte-Sanmiguel, N. Higuita-Castro and D. Gallego-Perez, in *Electroporation Protocols: Microorganism, Mammalian System, and Nanodevice*, ed. S. Li, L. Chang and J. Teissie, Springer US, 2020, pp. 79–84.
57 L. R. Lemmerman, *et al.*, Nanotransfection-based vasculogenic cell reprogramming drives functional recovery in a mouse model of ischemic stroke, *Sci. Adv.*, 2021, **7**(12), 1–11.
58 P. Bonaventura, *et al.*, Cold tumors: a therapeutic challenge for immunotherapy, *Front. Immunol.*, 2019, 10.
59 X. R. Ros and L. Vermeulen, Turning cold tumors hot by blocking TGF-β, *Trends Cancer*, 2018, **4**(5), 335–337.
60 E. Y. Lin, *et al.*, Progression to malignancy in the polyoma middle T oncoprotein mouse breast cancer model provides a reliable model for human diseases, *Am. J. Pathol.*, 2003, **163**(5), 2113–2126.
61 M. A. Forget, *et al.*, Macrophage colony-stimulating factor augments Tie2-expressing monocyte differentiation, angiogenic function, and recruitment in a mouse model of breast cancer, *PLoS One*, 2014, **9**(6), e98623.
62 D. Szklarczyk, *et al.*, STRING v11: protein-protein association networks with increased coverage, supporting functional discovery in genome-wide experimental datasets, *Nucleic Acids Res.*, 2019, **47**(D1), D607–D613.
63 L. Diaz-Starokozheva, *et al.*, Early Intervention in Ischemic Tissue with Oxygen Nanocarriers Enables Successful Implementation of Restorative Cell Therapies, *Cell. Mol. Bioeng.*, 2020, **13**(5), 435–446.
64 K. M. Pinckard, *et al.*, A Novel Endocrine Role for the BAT-Released Lipokine 12,13-diHOME to Mediate Cardiac Function, *Circulation*, 2021, **143**(2), 145–159.
65 D. Gallego-Perez, N. Higuita-Castro and L. Chang, Chandan Sen. Patent - interpenetrating microstructures for nanochannel - based CARGO delivery, *US Pat.*, US11235132B2, 2022.
66 J. Zhang, *et al.*, Immunomagnetic sequential ultrafiltration (iSUF) platform for enrichment and purification of extracellular vesicles from biofluids, *Sci. Rep.*, 2021, **11**(1), 8034.
67 M. Königshoff, *et al.*, WNT1-inducible signaling protein-1 mediates pulmonary fibrosis in mice and is upregulated in humans with idiopathic pulmonary fibrosis, *J. Clin. Invest.*, 2009, **119**(4), 772–787.